Superior Thermal Stability of High Energy Density and Power Density in Domain-Engineered $Bi_{0.5}Na_{0.5}TiO_3$−$NaTaO_3$ Relaxor Ferroelectrics

Xuefan Zhou, He Qi,* Zhongna Yan, Guoliang Xue, Hang Luo, and Dou Zhang*

State Key Laboratory of Powder Metallurgy, Central South University, Changsha, Hunan 410083, China

S Supporting Information

ABSTRACT: Thermal-stable dielectric capacitors with high energy density and power density have attracted increasing attention in recent years. In this work, $(1 − x)Bi_{0.5}Na_{0.5}TiO_3−xNaTaO_3$ [$(1 − x)$BNT−xNT, $x = 0−0.30$] lead-free relaxor ferroelectric ceramics are developed for capacitor applications. The $x = 0.20$ ceramic exhibits superior thermal stability of discharged energy density (W_D) with a variation of less than 10% in an ultrawide temperature range of −50 to 300 °C, showing a significant advantage compared with the previously reported ceramic systems. The W_D reaches 4.21 J/cm³ under 38 kV/mm at room temperature. Besides, a record high of power density ($P_D \approx 89.5$ MW/cm³) in BNT-based ceramics is also achieved in $x = 0.20$ ceramic with an excellent temperature insensitivity within 25−160 °C. The $x = 0.20$ ceramic is indicated to be an ergodic relaxor ferroelectric with coexisted $R3c$ nanodomains and $P4bm$ polar nanoregions at room temperature, greatly inducing large maximum polarization, maintaining low remnant polarization, and thus achieving high W_D and P_D. Furthermore, the diffuse phase transition from $R3c$ to $P4bm$ phase on heating is considered to be responsible for the superior thermal stability of the high W_D and P_D. These results imply the large potential of the 0.80BNT−0.20NT ceramic in temperature-stable dielectric capacitor applications.

KEYWORDS: thermal stability, energy storage, charge−discharge, $Bi_{0.5}Na_{0.5}TiO_3−NaTaO_3$ ceramic, polar nanoregions
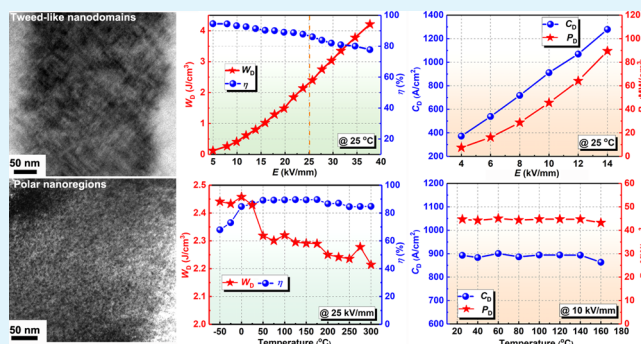
1. INTRODUCTION

Energy storage devices are essential to power electronic systems.[1−6] Dielectric capacitors have apparent benefits of high power density (P_D), pulse discharge, and excellent endurance, which are especially applicable for weapons, hybrid electric vehicles, and power electronics. However, dielectric capacitors usually show inferior energy density, which cannot meet the needs of integration and miniaturization and severely limits the further applications.[4] Generally, the energy storage parameters of dielectrics can be obtained by the electric displacement−electric field ($D−E$) loops, as shown below[5]

$$\text{Energy storage density } W = \int_0^{D_m} E \, dD \tag{1}$$

$$\text{Discharged energy density } W_D = \int_{D_r}^{D_m} E \, dD \tag{2}$$

$$\text{Energy efficiency } \eta = \frac{W_D}{W} \times 100\% \tag{3}$$

where D_m, D_r, and E denote the maximum electric displacement, remnant electric displacement, and applied electric field, respectively. Accordingly, a slim $D−E$ loop with large D_m, low

D_r, and high breakdown strength (E_B) is beneficial for energy storage performance.

Therefore, relaxor ferroelectrics are promising energy storage materials because of the large induced D_m, small D_r, and slim $D−E$ loops.[7−12] $Bi_{0.5}Na_{0.5}TiO_3$ (BNT), a typical lead-free relaxor ferroelectric, possesses a large D_m because of the similar electron configuration of Bi^{3+} (lone $6s^2$ electron) to that of Pb^{2+}.[13] However, the square $D−E$ loop of pure BNT with a high D_r is not conducive to energy storage. Through compositional modulation, such as heterovalent or isovalent ionic substitutions, the long-range ferroelectric order could be broken, and polar nanoregions (PNRs) are generated because of the large local random fields resulting from structural or charge inhomogeneities in a nanoscale. As a result, the ergodic relaxor state with PNRs and a slim $D−E$ loop can be achieved in BNT-based ceramics. In the past decade, many studies focused on the energy storage behaviors of BNT-based ceramic systems.[14−20] A record-high W_D of 7.02 J/cm³ was obtained in 0.78BNT−0.22NaNbO₃ ceramic.[17] Moreover, BNT-based ergodic relaxor ferroelectric ceramics are also attractive in

pulsed charge−discharge performance. By applying an electric field, the ergodic relaxor ferroelectrics with PNRs are converted into unstable ferroelectrics with long-range polar structures, which will quickly collapse after removing the electric field. The stored energy releases in a short time, generating a large P_D. Li et al. obtained a high current density (C_D) of 606 A/cm^2 and a P_D of 18.2 MW/cm^3 in 0.62BNT−0.06BaTiO$_3$−0.32(Sr$_{0.7}$Bi$_{0.2}$□$_{0.1}$)TiO$_3$ ceramics in the ergodic relaxor state.[21] Despite the achievements made so far, it is still challenging to achieve a large W_D in BNT-based bulk ceramics as most of the reported W_D is less than 3 J/cm^3, and investigations on the charge−discharge performance are limited at present, which is essential for applications.[13,21]

Furthermore, the thermal stability of W_D and P_D is also a significant concern of researchers,[4,19,22−27] which is critical for the reliable operation of dielectric capacitors in complex environments. For example, the power systems of hybrid electric vehicles may operate over the temperature range of −40 to 140 °C.[22] Thermal-stable dielectric capacitors in this temperature range will steadily work without the additional heating/cooling systems, which will be beneficial to improving the reliability and reducing the weight, volume, and cost. BNT-based relaxor ceramics are considered to be promising for thermal-stable dielectric capacitor applications because of their diffuse phase transition behaviors.[28−31] However, in the previously reported ceramics, the temperature range with stable energy storage and charge−discharge performance is usually limited within the room temperature (RT) ≈ 200 °C. A wider operational temperature range, including lower temperature below RT and higher temperatures above 200 °C, is necessary for the widespread applications of dielectric capacitors.

In this paper, the energy storage and charge−discharge performances of the $(1 − x)$BNT−xNaTaO$_3$ [$(1 − x)$BNT−xNT, x = 0−0.30] ceramic system were studied for the first time. NT is an incipient ferroelectric.[32,33] The introduction of Na$^+$ in the A sites and Ta^{5+} in the B- sites can effectively break the long-range polar ordering to generate PNRs, leading to enhanced ergodic relaxor behaviors and inducing diffused phase transitions. Thus, the high W_D and P_D with superior thermal stability were realized in BNT−NT ceramics. Finally, a high W_D of 4.21 J/cm^3 and an ultrahigh P_D of 89.5 MW/cm^3 are obtained in the 0.80BNT−0.20NT ceramic at RT. Besides, the W_D shows excellent thermal stability over an ultrawide temperature range of −50 to 300 °C, and the P_D is also stable within 25−160 °C. The superior thermal stability results from the diffuse phase transition on heating, which is revealed by the high-resolution transmission electron microscopy (HR-TEM) observation and in situ X-ray diffraction (XRD) results with changing temperature.

2. EXPERIMENTAL SECTION

$(1 − x)$BNT−xNT (x = 0−0.30) ceramics were fabricated by a solid-state reaction method using Bi$_2$O$_3$, Na$_2$CO$_3$, TiO$_2$, and Ta$_2$O$_5$ powders with 99.9% purity. The preparation processes are similar to those reported in our previous work.[34,35] The calcination of ceramic powders was performed at 800 °C for 2 h. The pressed ceramic pellets were sintered at 1160 °C for 2 h. The ceramics were crushed and ground into powders for crystal phase characterization. The XRD patterns at RT were tested by using a D8 ADVANCE X-ray diffractometer (Bruker AXS, Germany, Cu Kα radiation) with a step of 0.02° and a counting time of 2.5 s. Temperature-dependent XRD patterns were measured by using a SmartLab X-ray diffractometer (Rigaku, Japan, Cu Kα radiation) with a step of 0.02° at a speed of

2°/min. The ceramic powders were cooled or heated to a given temperature and held for 30 min. The temperature stability was controlled within 1 °C. The characterization of grain morphology, ferroelectric domains, and nanostructures is also similar to those reported in our previous work.[34,35]

Ag electrodes with a diameter of 2 mm were prepared on both sides of the ceramics with a thickness of 0.2 mm by annealing at 550 °C for 30 min. The D−E loops were measured at the frequency of 10 Hz by using a ferroelectric tester (TF Analyzer 2000, AixACCT systems, Germany). A precision impedance analyzer (4294A, Agilent Technologies, USA) was used to determine the dielectric properties. The charge−discharge properties were investigated by using a commercial charge−discharge platform (CFD-001, Gogo Instruments Technology, China) (see Figure S1).

3. RESULTS AND DISCUSSION

Figure 1a presents the XRD patterns of $(1 − x)$BNT−xNT (x = 0−0.30) ceramics measured at RT. All the ceramics
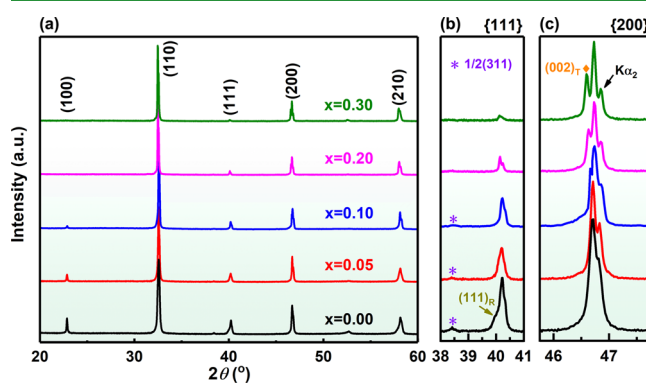

Figure 1. (a) XRD patterns of the $(1 − x)$BNT−xNT ceramics. Enlarged patterns in the 2θ ranges of (b) 38−41 and (c) 45.75−47.75°.

exhibited a single perovskite phase. The enlarged patterns in the 2θ ranges of 38−41 and 45.75−47.75° are given in Figure 1b,c, respectively. Regardless of the contribution from Cu Kα_2 radiation, the BNT ceramic exhibited a doublet {111} peak, a single {200} peak, and an obvious superstructure reflection at around 2θ = 38.3° indexed as 1/2(311), which are the evident features of the rhombohedral $R3c$ symmetry.[36,37] With the increase of the NT content from 0.00 to 0.10, the {111} peak became increasingly symmetrical, and the 1/2(311) peak gradually weakened. Moreover, an apparent splitting of the {200} peak was noticed for x = 0.10, indicating the tetragonal structure.[38] With the further increase of the NT content, the 1/2(311) peak was hard to be detected, and the (002)$_T$ peak was enhanced significantly. The results indicate the decreased rhombohedral phase and the enhanced tetragonal phase with the introduction of NT. In order to quantify the phases, Rietveld refinement was conducted by GSAS software. The optimal fits were obtained using the $R3c$ and $P4bm$ space groups (see Figure S2 and Table S1). The analysis results show that the $P4bm$ phase was gradually enhanced with the introduction of NT. Besides, it was found that the unit cell volumes gradually increased, which was attributed to the substitution of bigger ions (Na$^+$: 1.39 Å, Ta^{5+}: 0.64 Å) for smaller ions (Bi^{3+}: 1.36 Å, Ti^{4+}: 0.605 Å). The addition of NT had little effect on the grain size and morphology, as characterized by scanning electron microscopy (SEM). The SEM image of the x = 0.20 ceramic can be found in Figure S3, showing an average grain size of ∼3 μm.
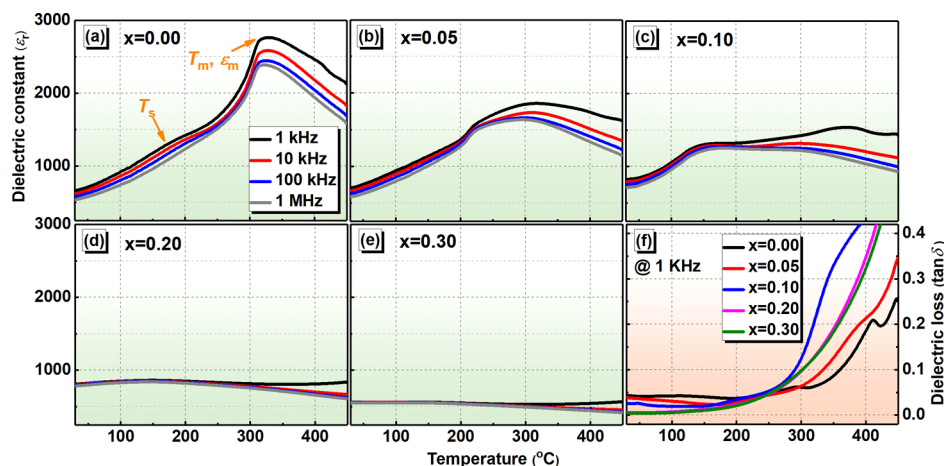
Figure 2. (a−e) Temperature-dependent ε_r and (f) tan δ of the $(1 − x)$BNT−xNT ceramics.

Figure 2a−e presents the variation of dielectric constant ε_r with temperature and frequency for the $(1 − x)$BNT−xNT ceramics. All the studied ceramics exhibited obvious dielectric relaxation.[35] For pure BNT ceramic, two dielectric anomalies can be detected. The first dielectric anomaly was a frequency-dispersive hump located at the lower temperature of T_s, which was reported to arise from the thermal evolution of $R3c$ and $P4bm$ PNRs.[39] The dielectric maximum (ε_m) located at T_m was the second dielectric anomaly. It can be seen that both ε_m and T_m decreased with the addition of NT, accompanied by the obvious broadening of the dielectric peak. The T_s also gradually decreased and dropped below RT when $x = 0.20$. The introduction of NT was believed to induce diffuse phase transitions and lead to apparently enhanced ergodicity at RT. The A-site substitution by Na$^+$ and B-site substitution by Ta^{5+} improved the chemical disorder because of the difference in radius and valence state of various cations, which could disrupt the long-range ferroelectric order and lead to a high random field in the ceramics. Moreover, it was noticed that the improved thermal stability of ε_r was achieved with the addition of NT. The $x = 0.20$ and 0.30 ceramics exhibited temperature-stable ε_r versus T curves. Figure 2f shows that the dielectric loss tan δ at RT for all the ceramics was below 0.05 and gradually decreased with the addition of NT.

Figure 3a,b presents the D−E loops and current density (I−E) curves measured under 10 kV/mm. The well-saturated D−E loop was observed for pure BNT ceramic, which became more and more pinched with the addition of NT. The BNT ceramic showed two sharp I−E peaks, which can be attributed to the reversal of ferroelectric domains at the coercive field (E_c), indicating the transition from the nonergodic relaxor state to the stable long-range ferroelectric state. The appearance of four I−E peaks at $\pm E_F$ and $\pm E_1$ when $x = 0.05$ implied the coexisted nonergodicity and ergodicity. In this case, with the removal of the electric field, the induced ferroelectric order returned to the initial ergodic state, leading to the current peak at $−E_1$. On the other hand, the current peak at $−E_F$ represented the back switching of the induced ferroelectric state from the initial nonergodic state. Moreover, no obvious current peak was detected when $x = 0.10$, 0.20, and 0.30. The results confirmed the enhanced ergodicity and suppressed ferroelectricity with the addition of NT. Figure 3c gives the evolution of D_m, D_r, and $D_m−D_r$ with the increase of the NT content. The D_m and D_r monotonously decreased, and high
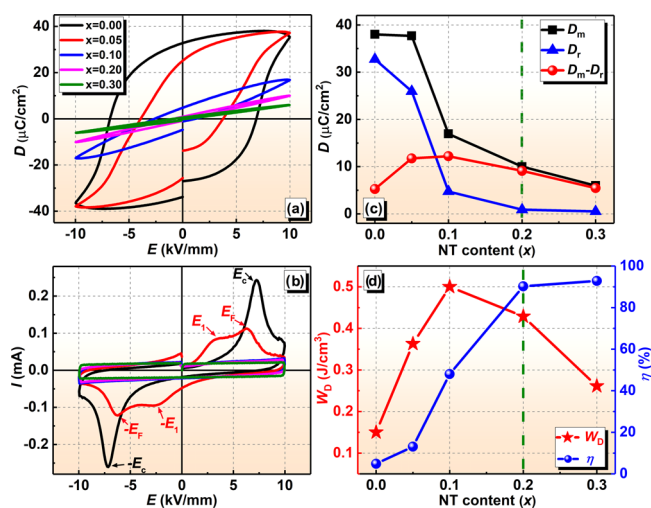

Figure 3. (a) D−E loops and (b) corresponding I−E curves of $(1 − x)$BNT−xNT ceramics. Evolution of (c) D_m, D_r, and $D_m−D_r$, and (d) W_D and η values with the addition of NT.

$D_m−D_r$ was obtained when $x = 0.05−0.20$. Besides, the $x = 0.10$ and 0.20 ceramics were found to exhibit large W_D of 0.50 and 0.43 J/cm^3, respectively, as shown in Figure 3d. However, both outstanding W_D and η are of importance in practical applications. The $x = 0.10$ ceramic showed a hysteretic D−E loop, leading to a low η of 48%. In contrast, a high η of 91% was achieved when $x = 0.20$, attributing to its low hysteresis of polarization response. Taking into account both W_D and η, the $x = 0.20$ ceramic is most promising in energy storage applications. Furthermore, it was noticed that the $x = 0.20$ ceramic possessed moderate ε_r of ~800 and particularly low tan δ of ~0.006 at RT, which are favorable for high E_B. It implies that the polarization of $x = 0.20$ ceramic would be further enhanced by increasing electric field, resulting in a larger W_D.

To thoroughly clarify the sources of excellent energy storage performance in the $x = 0.20$ ceramic, contact mode piezoresponse force microscopy (PFM) was used to study the domain structures of $(1 − x)$BNT−xNT ($x = 0.00−0.20$) ceramics at RT, as shown in Figure 4. The contrast in PFM amplitude images exhibits the strength of piezoresponse, while the polarization orientation is revealed by the PFM phase images. The $x = 0.00$ ceramic showed long-range-ordered
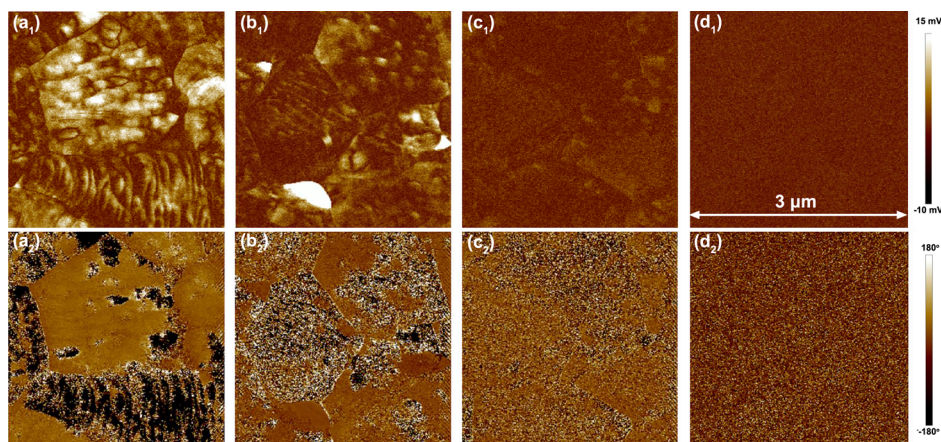
Figure 4. Out-of-plane PFM amplitude (subscript 1) and phase (subscript 2) images of the $(1 - x)$BNT$-x$NT ceramics: (a) $x = 0.00$, (b) $x = 0.05$, (c) $x = 0.10$, and (d) $x = 0.20$.
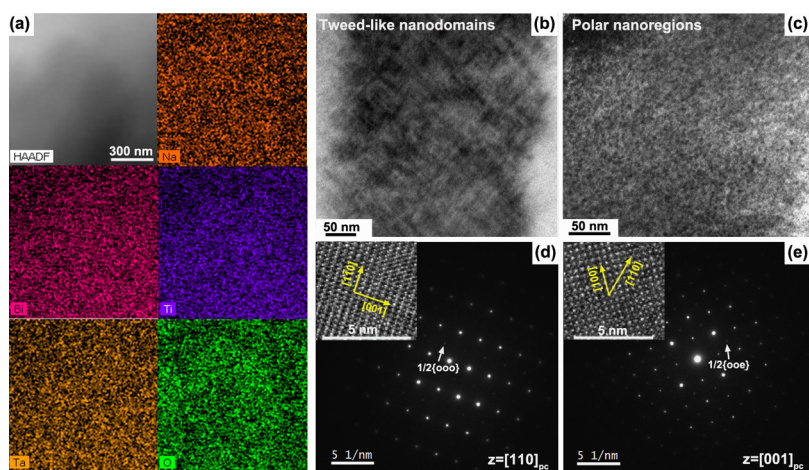

Figure 5. (a) HAADF and EDS mapping images of a typical grain in the $x = 0.20$ ceramic, (b,c) Bright-field TEM images of nanodomains in the $x = 0.20$ ceramic, and (d,e) SAED patterns along $[110]_{pc}$ and $[111]_{pc}$ orientations and corresponding HR-TEM images.

lamellar ferroelectric domains with strong and clear contrasts. The introduction of NT led to the smaller and blurred ferroelectric domains and the reduced piezoresponse amplitude. Especially, no clear patterns of domain structures can be observed when $x = 0.20$ because of the tiny nanodomains or PNRs. It is proved that the introduction of NT can cause an obvious decrease in size and increase in dynamics of domains, in favor of the enhancement of energy storage properties. For large-sized ferroelectric domains, a lot of energy will be absorbed by domain aligning and switching in the charge−discharge process and stored as remanence. In contrast, the fast response to the external electric field of small-sized and active PNRs will result in nearly hysteresis-free polarization responses and high W_D and η.

The nanostructure details in the $x = 0.20$ ceramic were further analyzed by the HR-TEM. Figure 5a gives the high-angle annular dark-field (HAADF) image and energy dispersive spectrometer (EDS) mapping images of a typical grain in the $x = 0.20$ ceramic. The constituent elements Na, Bi, Ti, Ta, and O were uniformly distributed in the grain. It directly indicates the complete diffusion of Ta into the lattice matrix. Figure 5b,c shows the bright-field TEM images of nanodomains in the $x = 0.20$ ceramic at RT. The clear contrast change demonstrates the presence of tweedlike nanodomains (10−20 nm) and PNRs (∼5 nm), which cannot be detected by

PFM. Figure 5d,e presents the selected area electron diffraction (SAED) patterns along $[110]_{pc}$ and $[001]_{pc}$ orientations, respectively. The insets give the corresponding HR-TEM images. The clear lattice fringes indicate the excellent crystallinity of the ceramic. The SAED patterns exhibited the 1/2{ooo} and 1/2{ooe} superlattice reflections (where o and e stand for the odd and even values of Miller indices, respectively). It was known that the 1/2{ooo} spots result from the antiphase $a^-a^-a^-$ oxygen octahedral tilting and are indicative of a $R3c$ phase, while the 1/2{ooe} spots represent the in-phase $a^0a^0c^+$ oxygen octahedral tilting and a $P4bm$ phase.[40] Therefore, we can conclude that $R3c$ and $P4bm$ symmetries were both involved in this composition. These nanodomains and PNRs can help to induce large D_m, maintain low D_r, and achieve high D_m-D_r in the $x = 0.20$ ceramic when applying an external electric field.

The energy storage behaviors of the $x = 0.20$ ceramic were studied carefully in this study. High E_B is essential to obtain advanced energy storage properties. The electric-field-dependent $D-E$ loops of the $x = 0.20$ ceramic were presented in Figure 6a. Figure 6b,c summarizes the variation of D_m, D_r, D_m-D_r, W_D, and η with electric field. The D_m-D_r increased from 4.5 to 27.2 μC/cm^3 with raising the electric field from 5 to 38 kV/mm. Accordingly, the W_D increased from 0.12 to 4.21 J/cm^3. However, the η visibly deteriorated from 94.5 to 77.8%.
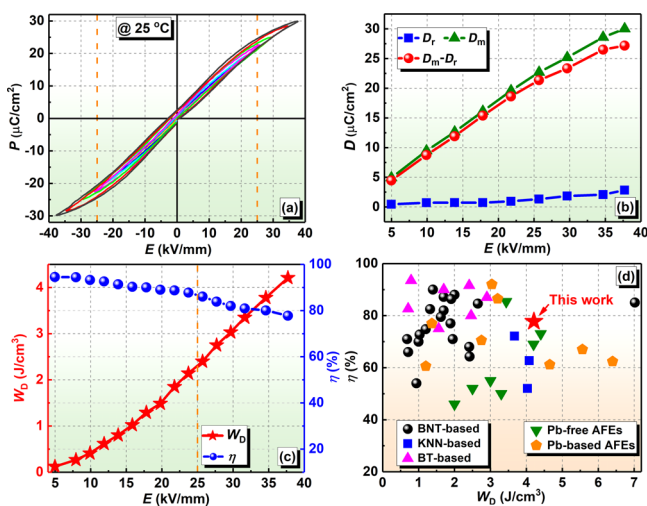
Figure 6. Electric-field-dependent (a) $D-E$ loops, (b) D_m, D_r, and D_m-D_r, (c) W_D, and η of the $x = 0.20$ ceramics, and (d) Energy storage properties of the $x = 0.20$ ceramic and recently reported ceramic systems [KNN: (K,Na)NbO$_3$, BT: BaTiO$_3$].

The strong electric field would induce enhanced domain switching and cause large polarization loss, which is responsible for the reduced η. The nearly linear $D-E$ loops were obtained under lower electric fields, proving that there is no noticeable domain switching or phase transition. A more hysteretic $D-E$ loop was formed under the electric field of more than 25 kV/mm, accompanied by the apparent reduction of η. It was supposed that a high enough electric field would induce the formation of long-range polar ordering through phase switching. Nevertheless, a high W_D of 4.21 J/cm^3 and a

desirable η of 77.8% were obtained simultaneously in this work. The energy storage properties of the $x = 0.20$ ceramic were compared with the recently reported ceramic systems,[3−12,14−19,41−47] as shown in Figure 6d. We noticed that large W_D can be obtained in antiferroelectrics (AFEs). However, their η is usually low because the AFE-ferroelectric phase transition under electric field also brings evident hysteresis and large energy loss. It is highly desirable to improve the W_D and η simultaneously. By comparison, the $x = 0.20$ relaxor ferroelectric ceramic reaches a superior balance between W_D and η.

Temperature stability is also crucial in ensuring the reliable operation of dielectric capacitors in harsh environments. The temperature-dependent ε_r and tan δ of the $x = 0.20$ ceramic were measured from −100 to 500 °C, as given in Figure 7a. It can be seen that the T_s was located at about −50 to −30 °C and T_m was located at about 150 °C with a highly broadened dielectric peak, which can be attributed to its large local random field, highly-dynamic and small-sized PNRs, as discussed before. Excellent dielectric temperature stability was achieved. Figure 7b gives the temperature-dependent $\Delta\varepsilon_r/\varepsilon_{r\ 25°C}$. Significantly, the observed change of ε_r was within 10% over an ultrawide temperature range of −50 to 350 °C for all measured frequencies, accompanied by a low tan δ. It implies that the $x = 0.20$ ceramic could be an ideal candidate for temperature-stable dielectric capacitor applications.

The thermal stability of W_D and η was subsequently measured. Figure 7c presents the temperature-dependent $D-E$ loops within −50 to 300 °C under 25 kV/mm. Notably, the $D-E$ loops at −50 and −25°C show visible hysteresis, while extremely low hysteresis was observed within 0−300 °C. Moreover, the D_m and D_r first decreased with temperature raising from −50 to 50 °C and then remained almost stable
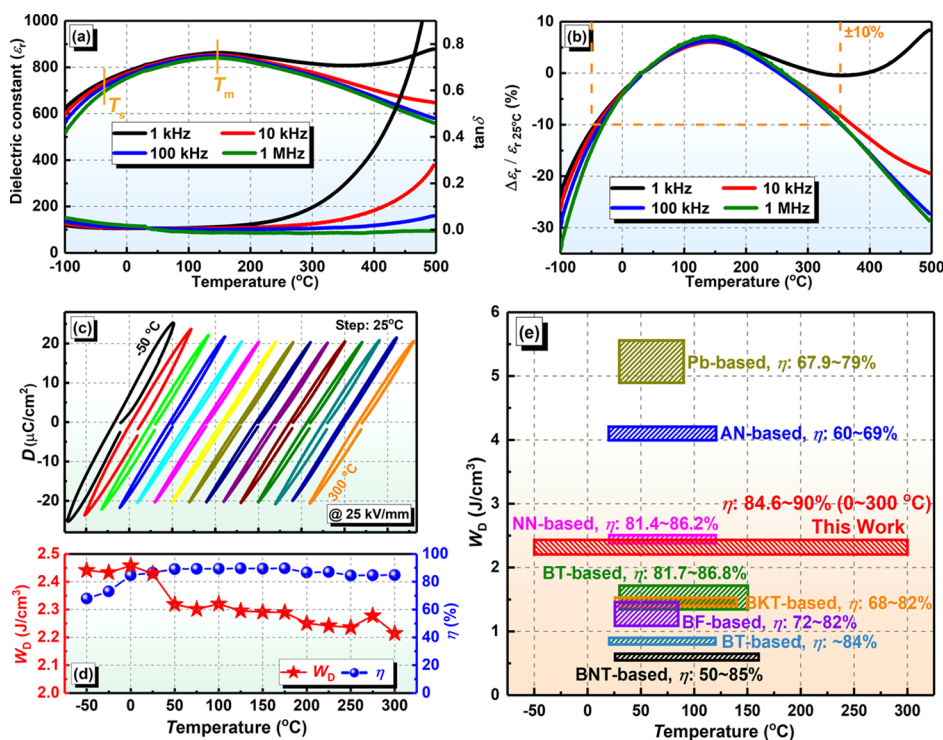

Figure 7. (a) Temperature-dependent ε_r, tan δ and (b) $\Delta\varepsilon_r/\varepsilon_{r\ 25°C}$ of the $x = 0.20$ ceramic. (c) Temperature-dependent $D-E$ loops and (d) corresponding W_D and η. (e) Temperature-dependent W_D and η of the $x = 0.20$ ceramic and recently reported ceramics (BF: BiFeO$_3$, BKT: Bi$_{0.5}$K$_{0.5}$TiO$_3$, NN: NaNbO$_3$, and AN: AgNbO$_3$).

until 300 °C. In the low-temperature region (lower than 0 °C), the local random fields could be overcome under 25 kV/mm, causing the domain switching and phase transition, which resulted in a larger polarization hysteresis, D_m and D_r. In contrast, the linearlike $D-E$ loops within 0−300 °C imply that no visible domain switching occurred under 25 kV/mm owing to the increase of the random field upon heating. The evolution of W_D and η with the increase of temperature is summarized in Figure 7d. Because of the lower dynamic of PNRs at −50 and −25 °C, the η was relatively lower, that is, 68 and 73%, respectively. However, the η can be kept within 84.5−90% in a wide temperature range of 0−300 °C. A slightly reduced η at high temperatures may result from the conduction loss. Furthermore, the W_D within −50 to 25°C was found to be slightly higher than that within 50−300 °C owing to the relatively larger D_m-D_r. Significantly, the variation of W_D was lower than 10% within −50 to 300 °C (W_D: 2.22−2.45 J/cm^3). Figure 7e exhibits the temperature-dependent W_D and η of the $x = 0.20$ ceramic and recently reported ceramics.[4,19,22−27] The previously reported ceramics usually exhibited the thermal-stable energy density above RT and below 200 °C, while the $x = 0.20$ ceramic in this work showed much better stability over a wider temperature range of −50 to 300 °C. Even though some AFE ceramics exhibited larger W_D than the $x = 0.20$ ceramic, their hysteretic AFE-ferroelectric phase transition during the charge−discharge process inevitably resulted in relatively low η. These results fully reflect the superiority of the $x = 0.20$ ceramic in temperature-stable dielectric capacitor applications.

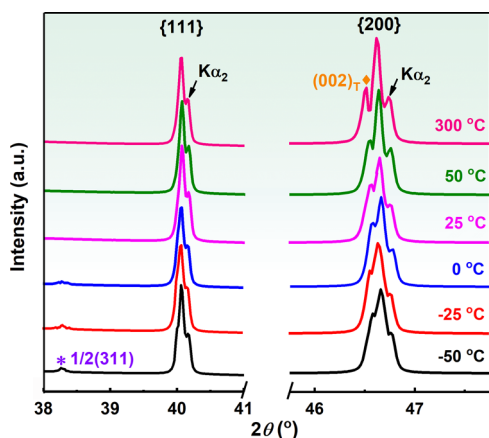The phase evolution of the $x = 0.20$ ceramic with the increase of temperature was examined in this work. Figure 8

Figure 8. Magnified XRD patterns in the 2θ ranges of 38−41 and 45.75−47.75° of the $x = 0.20$ ceramic measured from −50 to 300 °C.

displays the magnified XRD patterns in the 2θ ranges of 38−41 and 45.75−47.75° of the $x = 0.20$ ceramic measured from −50 to 300 °C. In the temperature range of −50 to 0 °C, a distinct 1/2(311) superlattice peak and a weak (002)$_T$ peak were detected, revealing the presence of $R3c$ and $P4bm$ phases. With the increase of temperature, the (002)$_T$ peak was intensified significantly, suggesting an increase in the tetragonality of the lattice. Besides, there was no detectable 1/2(311) superlattice peak in the temperature range of 25−300 °C. Considering the TEM results shown in Figure 5, it was believed that the $R3c$ and $P4bm$ phases coexisted within −50 to 25 °C, and a pure $P4bm$ phase was obtained at 50 °C and kept until at least 300

°C. For clarifying the phase constitution at various temperatures, the Rietveld refinement was also carried out (see Figure S4 and Table S2). The fitting analysis shows that the $P4bm$ phase fraction monotonously increased from 47.3 to 92.5%, while the $R3c$ phase fraction decreased from 52.7 to 7.5% with temperature raising from −50 to 25 °C. The hysteretic $D-E$ loops with large D_m and D_r at −50 and −25 °C could be attributed to the relatively high content of larger-sized PNRs or nanodomains with the $R3c$ phase in these cases. The enhanced content of smaller-sized $P4bm$ PNRs was responsible for the decreased hysteresis, D_m, and D_r with increasing temperature, as given in Figure 7c. Furthermore, the stable low-hysteresis linearlike polarization response in the temperature range of 50−300 °C could be attributed to the pure $P4bm$ PNRs. Consequently, the diffused phase transitions significantly contributed to the stable polarization and dielectric responses with the variation of temperature. Therefore, the superior thermal-stable energy storage property was achieved in the $x = 0.20$ ceramic.

From a practical point of view, the charge−discharge behaviors of the $x = 0.20$ ceramic were also evaluated. Figure 9a presents the electric-field-dependent underdamped discharge curves at RT. With the increasing electric field, the $x = 0.20$ ceramic showed similar discharging behaviors, whereas the first peak was gradually enhanced. The stored charge was released rapidly (<0.2 μs). Besides, some important discharging parameters can be obtained from these underdamped discharge waveforms, including

$$\text{Current density } C_D = \frac{I_{max}}{S} \quad (4)$$

$$\text{Power density } P_D = \frac{EI_{max}}{2S} \quad (5)$$

where I_{max} and S, respectively, represent the peak current and electrode area, and E is the electric field.[5] The variation of C_D and P_D with electric field was given in Figure 9b. The C_D monotonously increased from 372 to 1278 A/cm^2. Significantly, a record high of P_D (~89.5 MW/cm^3) in BNT-based ceramics was achieved in the $x = 0.20$ ceramic. The charge−discharge performance of the recently reported ceramic systems[5,21,22,24,48−54] was summarized in Table S3.

Considering the equation[54]

$$\frac{I_{max}}{S} = \frac{\mathrm{d}Q_{max}}{S\,\mathrm{d}t} = \frac{\mathrm{d}P_{max}}{\mathrm{d}t} \quad (6)$$

where the large C_D of the $x = 0.20$ ceramic should be attributed to the high induced polarization and short release time. Besides, the large working electric field of 14 kV/mm is also responsible for the large P_D, which is a distinct advantage of the $x = 0.20$ ceramic compared with traditional lead-based AFE ceramics. The $x = 0.20$ ceramic was proved to be an ergodic relaxor ferroelectric at RT and possesses coexisted $R3c$ and $P4bm$ phases with nanodomains and PNRs, leading to its large working electric field, high induced polarization, and fast charge−discharge rate. Furthermore, we investigated the temperature-dependent underdamped discharge properties under 10 kV/mm, as shown in Figure 9c,d. The $x = 0.20$ ceramic exhibited thermal-stable underdamped discharge waveforms over 25−160 °C. Both C_D and P_D changed slightly in the studied temperature range. The $x = 0.20$ ceramic deserves more attention and consideration for application in the pulsed power technology.
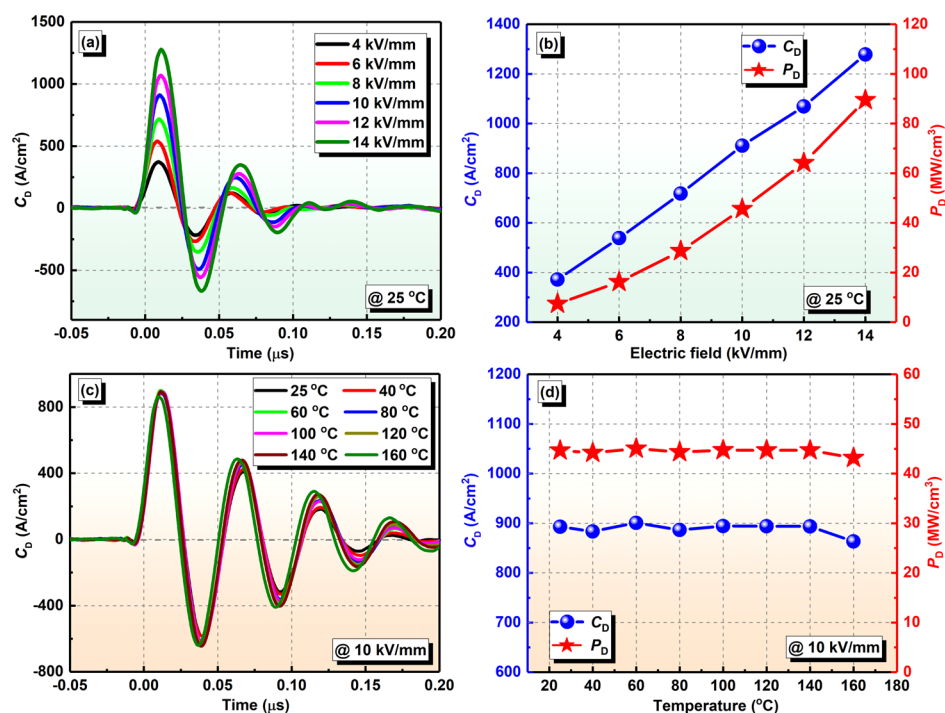
Figure 9. (a) Underdamped discharge waveforms of the $x = 0.20$ ceramic over 4−14 kV/mm. (b) Variation of C_D and P_D with electric field. (c) Underdamped discharge waveforms over 25−160 °C. (d) Variation of C_D and P_D with temperature.

4. CONCLUSIONS

In summary, the lead-free $(1 − x)$BNT−xNT ceramics were studied for dielectric capacitor applications. The introduction of NT into BNT led to the nonergodic−ergodic relaxor phase transition. The lamellar microdomains also evolved to PNRs. Owing to the fast response of $R3c$ nanodomains and $P4bm$ PNRs in the $x = 0.20$ ceramic, a high W_D of 4.21 J/cm³ was generated under 38 kV/mm at RT. More significantly, the $x = 0.20$ ceramic possesses excellent thermally insensitive W_D with a variation of less than 10% over an ultrawide temperature range of −50 to 300 °C. Besides, an ultrahigh P_D of 89.5 MW/cm³ was also achieved in the $x = 0.20$ ceramic at RT, accompanied by favorable temperature stability within 25−160 °C. The diffuse phase transition from $R3c$ to $P4bm$ PNRs was considered to be the origin of the superior of high W_D and P_D. These outstanding energy storage and charge−discharge properties make the 0.80BNT−0.20NT ceramic an attractive material in temperature-stable dielectric capacitor applications.

ASSOCIATED CONTENT

Ⓢ Supporting Information

The Supporting Information is available free of charge on the ACS Publications website at DOI: 10.1021/acsami.9b13215.

> Schematic diagram of the charge−discharge measuring system; Rietveld refinement results of XRD patterns for the $(1 − x)$BNT−xNT ceramics measured at RT; Refined lattice parameters by the Rietveld method for the $(1 − x)$BNT−xNT ceramics measured at RT; SEM image of the $x = 0.20$ ceramic; Rietveld refinement results of XRD patterns for the $x = 0.20$ ceramic measured at various temperatures; Refined lattice parameters by the Rietveld method for the $x = 0.20$ ceramics measured at various temperatures; and comparison of charge−discharge properties among different ceramic systems (PDF)

AUTHOR INFORMATION

Corresponding Authors
*E-mail: qihehfut@163.com (H.Q.).
*E-mail: dzhang@csu.edu.cn (D.Z.).

ORCID Ⓘ
He Qi: 0000-0002-3094-3574
Dou Zhang: 0000-0001-8555-2784

Notes
The authors declare no competing financial interest.

ACKNOWLEDGMENTS

REFERENCES

(1) Yao, Z.; Song, Z.; Hao, H.; Yu, Z.; Cao, M.; Zhang, S.; Lanagan, M. T.; Liu, H. Homogeneous/Inhomogeneous-Structured Dielectrics and their Energy-Storage Performances. *Adv. Mater.* **2017**, *29*, 1601727.

(2) Luo, H.; Zhou, X.; Ellingford, C.; Zhang, Y.; Chen, S.; Zhou, K.; Zhang, D.; Bowen, C. R.; Wan, C. Interface Design for High Energy Density Polymer Nanocomposites. *Chem. Soc. Rev.* **2019**, *48*, 4424−4465.

(3) Peddigari, M.; Palneedi, H.; Hwang, G.-T.; Lim, K. W.; Kim, G.-Y.; Jeong, D.-Y.; Ryu, J. Boosting the Recoverable Energy Density of Lead-Free Ferroelectric Ceramic Thick Films through Artificially Induced Quasi-Relaxor Behavior. *ACS Appl. Mater. Interfaces* **2018**, *10*, 20720−20727.

(4) Zhao, L.; Liu, Q.; Gao, J.; Zhang, S.; Li, J.-F. Lead-Free Antiferroelectric Silver Niobate Tantalate with High Energy Storage Performance. *Adv. Mater.* **2017**, *29*, 1701824.

(5) Zhou, M.; Liang, R.; Zhou, Z.; Dong, X. Novel $BaTiO_3$-Based Lead-Free Ceramic Capacitors Featuring High Energy Storage Density, High Power Density, and Excellent Stability. *J. Mater. Chem. C* 2018, 6, 8528−8537.

(6) Zhang, L.; Jiang, S.; Fan, B.; Zhang, G. Enhanced Energy Storage Performance in $(Pb_{0.858}Ba_{0.1}La_{0.02}Y_{0.008})(Zr_{0.65}Sn_{0.3}Ti_{0.05})O_3$-$(Pb_{0.97}La_{0.02})(Zr_{0.9}Sn_{0.05}Ti_{0.05})O_3$ Anti-Ferroelectric Composite Ceramics by Spark Plasma Sintering. *J. Alloys Compd.* 2015, 622, 162−165.

(7) Yin, J.; Zhang, Y.; Lv, X.; Wu, J. Ultrahigh Energy-Storage Potential under Low Electric Field in Bismuth Sodium Titanate-Based Perovskite Ferroelectrics. *J. Mater. Chem. A* 2018, 6, 9823−9832.

(8) Chen, P.; Chu, B. Improvement of Dielectric and Energy Storage Properties in $Bi(Mg_{1/2}Ti_{1/2})O_3$-Modified $(Na_{1/2}Bi_{1/2})_{0.92}Ba_{0.08}TiO_3$ Ceramics. *J. Eur. Ceram. Soc.* 2016, 36, 81−88.

(9) Xu, Q.; Li, T.; Hao, H.; Zhang, S.; Wang, Z.; Cao, M.; Yao, Z.; Liu, H. Enhanced Energy Storage Properties of $NaNbO_3$ Modified $Bi_{0.5}Na_{0.5}TiO_3$ Based Ceramics. *J. Eur. Ceram. Soc.* 2015, 35, 545−553.

(10) Mishra, A.; Majumdar, B.; Ranjan, R. A Complex Lead-Free $(Na, Bi, Ba)(Ti, Fe)O_3$ Single Phase Perovskite Ceramic with a High Energy-Density and High Discharge-Efficiency for Solid State Capacitor Applications. *J. Eur. Ceram. Soc.* 2017, 37, 2379−2384.

(11) Tao, C.-W.; Geng, X.-Y.; Zhang, J.; Wang, R.-X.; Gu, Z.-B.; Zhang, S.-T. $Bi_{0.5}Na_{0.5}TiO_3$-$BaTiO_3$-$K_{0.5}Na_{0.5}NbO_3$:ZnO Relaxor Ferroelectric Composites with High Breakdown Electric Field and Large Energy Storage Properties. *J. Eur. Ceram. Soc.* 2018, 38, 4946−4952.

(12) Pan, Z.; Hu, D.; Zhang, Y.; Liu, J.; Shen, B.; Zhai, J. Achieving High Discharge Energy Density and Efficiency with NBT-Based Ceramics for Application in Capacitors. *J. Mater. Chem. C* 2019, 7, 4072−4078.

(13) Wu, Y.; Fan, Y.; Liu, N.; Peng, P.; Zhou, M.; Yan, S.; Cao, F.; Dong, X.; Wang, G. Enhanced Energy Storage Properties in Sodium Bismuth Titanate-Based Ceramics for Dielectric Capacitor Applications. *J. Mater. Chem. C* 2019, 7, 6222−6230.

(14) Wu, J.; Mahajan, A.; Riekehr, L.; Zhang, H.; Yang, B.; Meng, N.; Zhang, Z.; Yan, H. Perovskite $Sr_x(Bi_{1-x}Na_{0.97-x}Li_{0.03})_{0.5}TiO_3$ Ceramics with Polar Nanoregions for High Power Energy Storage. *Nano Energy* 2018, 50, 723−732.

(15) Hu, B.; Fan, H.; Ning, L.; Gao, S.; Yao, Z.; Li, Q. Enhanced Energy-Storage Performance and Dielectric Temperature Stability of $(1-x)(0.65Bi_{0.5}Na_{0.5}TiO_3$-$0.35Bi_{0.1}Sr_{0.85}TiO_3)$-$xKNbO_3$ Ceramics. *Ceram. Int.* 2018, 44, 10968−10974.

(16) Cao, W.; Li, W.; Feng, Y.; Bai, T.; Qiao, Y.; Hou, Y.; Zhang, T.; Yu, Y.; Fei, W. Defect Dipole Induced Large Recoverable Strain and High Energy-Storage Density in Lead-Free $Na_{0.5}Bi_{0.5}TiO_3$-Based Systems. *Appl. Phys. Lett.* 2016, 108, 202902.

(17) Qi, H.; Zuo, R. Linear-Like Lead-Free Relaxor Antiferroelectric $(Bi_{0.5}Na_{0.5})TiO_3$-$NaNbO_3$ with Giant Energy Storage Density/Efficiency and Super Stability against Temperature and Frequency. *J. Mater. Chem. A* 2019, 7, 3971−3978.

(18) Yan, F.; Yang, H.; Ying, L.; Wang, T. Enhanced Energy Storage Properties of a Novel Lead-Free Ceramic with a Multilayer Structure. *J. Mater. Chem. C* 2018, 6, 7905−7912.

(19) Li, F.; Zhai, J.; Shen, B.; Liu, X.; Yang, K.; Zhang, Y.; Li, P.; Liu, B.; Zeng, H. Influence of Structural Evolution on Energy Storage Properties in $Bi_{0.5}Na_{0.5}TiO_3$-$SrTiO_3$-$NaNbO_3$ Lead-Free Ferroelectric Ceramics. *J. Appl. Phys.* 2017, 121, 054103.

(20) Li, J.; Li, F.; Xu, Z.; Zhang, S. Multilayer Lead-Free Ceramic Capacitors with Ultrahigh Energy Density and Efficiency. *Adv. Mater.* 2018, 30, 1802155.

(21) Li, F.; Yang, K.; Liu, X.; Zou, J.; Zhai, J.; Shen, B.; Li, P.; Shen, J.; Liu, B.; Chen, P.; Zhao, K.; Zeng, H. Temperature Induced High Charge-Discharge Performances in Lead-Free $Bi_{0.5}Na_{0.5}TiO_3$-Based Ergodic Relaxor Ferroelectric Ceramics. *Scr. Mater.* 2017, 141, 15−19.

(22) Yuan, Q.; Yao, F.; Wang, Y.; Ma, R.; Wang, H. Relaxor Ferroelectric $0.9BaTiO_3$-$0.1Bi(Zn_{0.5}Zr_{0.5})O_3$ Ceramic Capacitors with High Energy Density and Temperature Stable Energy Storage Properties. *J. Mater. Chem. C* 2017, 5, 9552−9558.

(23) Li, W.-B.; Zhou, D.; Pang, L.-X.; Xu, R.; Guo, H.-H. Novel Barium Titanate Based Capacitors with High Energy Density and Fast Discharge Performance. *J. Mater. Chem. A* 2017, 5, 19607−19612.

(24) Zhou, M.; Liang, R.; Zhou, Z.; Dong, X. Superior Energy Storage Properties and Excellent Stability of Novel $NaNbO_3$-Based Lead-Free Ceramics with A-Site Vacancy Obtained Via a Bi_2O_3 Substitution Strategy. *J. Mater. Chem. A* 2018, 6, 17896−17904.

(25) Li, F.; Jiang, T.; Zhai, J.; Shen, B.; Zeng, H. Exploring Novel Bismuth-Based Materials for Energy Storage Applications. *J. Mater. Chem. C* 2018, 6, 7976−7981.

(26) Liu, N.; Liang, R.; Zhou, Z.; Dong, X. Designing Lead-Free Bismuth Ferrite-Based Ceramics Learning From Relaxor Ferroelectric Behavior for Simultaneous High Energy Density and Efficiency under Low Electric Field. *J. Mater. Chem. C* 2018, 6, 10211−10217.

(27) Zhang, Q.; Tong, H.; Chen, J.; Lu, Y.; Yang, T.; Yao, X.; He, Y. High Recoverable Energy Density over a Wide Temperature Range in Sr Modified $(Pb,La)(Zr,Sn,Ti)O_3$ Antiferroelectric Ceramics with an Orthorhombic Phase. *Appl. Phys. Lett.* 2016, 109, 262901.

(28) Ren, P.; He, J.; Wang, X.; Wan, Y.; Yan, F.; Zhao, G. High-Temperature Dielectrics Based on $(1 - x)[0.94Bi_{0.5}Na_{0.5}TiO_3$-$0.06BaTiO_3$-$0.03AgNbO_3]$-$xK_{0.5}Na_{0.5}NbO_3$. *J. Mater. Sci.: Mater. Electron.* 2018, 29, 17016−17021.

(29) Acosta, M.; Zang, J.; Jo, W.; Rödel, J. High-Temperature Dielectrics in $CaZrO_3$-Modified $Bi_{1/2}Na_{1/2}TiO_3$-Based Lead-Free Ceramics. *J. Eur. Ceram. Soc.* 2012, 32, 4327−4334.

(30) Su, C.; Hao, H.; Xu, Q.; Lu, Y.; Appiah, M.; Diao, C.; Cao, M.; Yao, Z.; Liu, H. Manufacture and Dielectric Properties of X9R Bi-Based Lead-Free Multilayer Ceramic Capacitors with AgPd Inner Electrodes. *J. Mater. Sci.: Mater. Electron.* 2016, 27, 6140−6149.

(31) Höfling, M.; Steiner, S.; Hoang, A.-P.; Seo, I.-T.; Frömling, T. Optimizing the Defect Chemistry of $Na_{1/2}Bi_{1/2}TiO_3$-Based Materials: Paving the Way for Excellent High Temperature Capacitors. *J. Mater. Chem. C* 2018, 6, 4769−4776.

(32) Tkach, A.; Almeida, A.; Moreira, J. A.; Perez de la Cruz, J.; Romaguera-Barcelay, Y.; Vilarinho, P. M. Low-Temperature Dielectric Response of $NaTaO_3$ Ceramics and Films. *Appl. Phys. Lett.* 2012, 100, 192909.

(33) Künig, J.; Jancar, B.; Suvorov, D. New $Na_{0.5}Bi_{0.5}TiO_3$-$NaTaO_3$-Based Perovskite Ceramics. *J. Am. Ceram. Soc.* 2007, 90, 3621−3627.

(34) Zhou, X.; Qi, H.; Yan, Z.; Xue, G.; Luo, H.; Zhang, D. Large Energy Density with Excellent Stability in Fine-Grained $(Bi_{0.5}Na_{0.5})$-TiO_3-Based Lead-Free Ceramics. *J. Eur. Ceram. Soc.* 2019, 39, 4053−4059.

(35) Zhou, X.; Yan, Z.; Qi, H.; Wang, L.; Wang, S.; Wang, Y.; Jiang, C.; Luo, H.; Zhang, D. Electrical Properties and Relaxor Phase Evolution of Nb-Modified $Bi_{0.5}Na_{0.5}TiO_3$-$Bi_{0.5}K_{0.5}TiO_3$-$SrTiO_3$ Lead-Free Ceramics. *J. Eur. Ceram. Soc.* 2019, 39, 2310−2317.

(36) Jones, G. O.; Thomas, P. A. Investigation of the Structure and Phase Transitions in the Novel A-site Substituted Distorted Perovskite Compound $Na_{0.5}Bi_{0.5}TiO_3$. *Acta Crystallogr.* 2002, 58, 168−178.

(37) Aksel, E.; Forrester, J. S.; Kowalski, B.; Jones, J. L.; Thomas, P. A. Phase Transition Sequence in Sodium Bismuth Titanate Observed Using High-Resolution X-ray Diffraction. *Appl. Phys. Lett.* 2011, 99, 222901.

(38) Jones, G. O.; Thomas, P. A. The Tetragonal Phase of $Na_{0.5}Bi_{0.5}TiO_3$ - a New Variant of the Perovskite Structure. *Acta Crystallogr.* 2000, 56, 426−430.

(39) Jo, W.; Schaab, S.; Sapper, E.; Schmitt, L. A.; Kleebe, H. J.; Bell, A. J.; Rödel, J. On the Phase Identity and Its Thermal Evolution of Lead Free $(Bi_{1/2}Na_{1/2})TiO_3$-6mol% $BaTiO_3$. *J. Appl. Phys.* 2011, 110, 074106.

(40) Woodward, D. I.; Reaney, I. M. Electron Diffraction of Tilted Perovskites. *Acta Crystallogr. B* 2005, 61, 387−399.

(41) Shao, T.; Du, H.; Ma, H.; Qu, S.; Wang, J.; Wang, J.; Wei, X.; Xu, Z. Significantly Enhanced Recoverable Energy Storage Density in

Potassium-Sodium Niobate-Based Lead Free Ceramics. *J. Mater. Chem. A* **2017**, *5*, 554−563.

(42) Zhao, L.; Gao, J.; Liu, Q.; Zhang, S.; Li, J.-F. Silver Niobate Lead-Free Antiferroelectric Ceramics: Enhancing Energy Storage Density by B-Site Doping. *ACS Appl. Mater. Interfaces* **2018**, *10*, 819−826.

(43) Shen, Z.; Wang, X.; Luo, B.; Li, L. $BaTiO_3$-$BiYbO_3$ Perovskite Materials for Energy Storage Applications. *J. Mater. Chem. A* **2015**, *3*, 18146−18153.

(44) Wu, L.; Wang, X.; Li, L. Lead-Free $BaTiO_3$-$Bi(Zn_{2/3}Nb_{1/3})O_3$ Weakly Coupled Relaxor Ferroelectric Materials for Energy Storage. *RSC Adv.* **2016**, *6*, 14273−14282.

(45) Li, W.-B.; Zhou, D.; Pang, L.-X. Enhanced Energy Storage Density by Inducing Defect Dipoles in Lead Free Relaxor Ferroelectric $BaTiO_3$-Based Ceramics. *Appl. Phys. Lett.* **2017**, *110*, 132902.

(46) Jo, H. R.; Lynch, C. S. A High Energy Density Relaxor Antiferroelectric Pulsed Capacitor Dielectric. *J. Appl. Phys.* **2016**, *119*, 024104.

(47) Zhang, Q.; Tong, H.; Chen, J.; Lu, Y.; Yang, T.; Yao, X.; He, Y. High Recoverable Energy Density over a Wide Temperature Range in Sr Modified $(Pb,La)(Zr,Sn,Ti)O_3$ Antiferroelectric Ceramics with an Orthorhombic Phase. *Appl. Phys. Lett.* **2016**, *109*, 262901.

(48) Xu, R.; Xu, Z.; Feng, Y.; He, H.; Tian, J.; Huang, D. Temperature Dependence of Energy Storage in $Pb_{0.90}La_{0.04}Ba_{0.04}[(Zr_{0.7}Sn_{0.3})_{0.88}Ti_{0.12}]O_3$ Antiferroelectric Ceramics. *J. Am. Ceram. Soc.* **2016**, *99*, 2984−2988.

(49) Zhang, H.; Chen, X.; Cao, F.; Wang, G.; Dong, X.; Hu, Z.; Du, T. Charge-Discharge Properties of an Antiferroelectric Ceramics Capacitor Under Different Electric Fields. *J. Am. Ceram. Soc.* **2010**, *93*, 4015−4017.

(50) Chen, X.; Zhang, H.; Cao, F.; Wang, G.; Dong, X.; Gu, Y.; He, H.; Liu, Y. Charge-Discharge Properties of Lead Zirconate Stannate Titanate Ceramics. *J. Appl. Phys.* **2009**, *106*, 034105.

(51) Xu, C.; Liu, Z.; Chen, X.; Yan, S.; Cao, F.; Dong, X.; Wang, G. High Charge-Discharge Performance of $Pb_{0.98}La_{0.02}(Zr_{0.35}Sn_{0.55}Ti_{0.10})_{0.995}O_3$ Antiferroelectric Ceramics. *J. Appl. Phys.* **2016**, *120*, 074107.

(52) Xu, R.; Tian, J.; Zhu, Q.; Zhao, T.; Feng, Y.; Wei, X.; Xu, Z. Effects of Phase Transition on Discharge Properties of PLZST Antiferroelectric Ceramics. *J. Am. Ceram. Soc.* **2017**, *100*, 3618−3625.

(53) Xu, R.; Xu, Z.; Feng, Y.; Wei, X.; Tian, J. Polarization of Antiferroelectric Ceramics for Pulse Capacitors under Transient Electric Field. *J. Appl. Phys.* **2016**, *120*, 144102.

(54) Xu, C.; Fu, Z.; Liu, Z.; Wang, L.; Yan, S.; Chen, X.; Cao, F.; Dong, X.; Wang, G. La/Mn codoped $AgNbO_3$ Lead-Free Antiferroelectric Ceramics with Large Energy Density and Power Density. *ACS Sustainable Chem. Eng.* **2018**, *6*, 16151−16159.